Fracture Mapping in the Soultz-sous-Forêts geothermal field from Microearthquake relocation

Sophie Michelet and M. Nafi Toksöz
Earth Resource Laboratory
Department of Earth, Atmospheric, and Planetary Sciences
Massachusetts Institute of Technology

Abstract

In 2003, a massive hydraulic fracturing experiment was carried out at the European Geothermal Hot Dry Rock site at Soultz-sous-Forêts, France. The two week injection of water generated a high level of microseismic activity. About 90,000 microearthquakes were triggered during and after this fluid injection. Of these, 21,000 events, detected at all stations, were located individually with a grid search algorithm to characterize the extent of the seismic zones and, ultimately, of the fracture network. The accuracy of these initial locations was around 70 meters, not sufficient to map detailed fracture patterns.

We undertook a relocation effort using two different techniques: Joint Hypocenter Determination (JHD) and Multiplet analysis. The JHD technique allows for the simultaneous location of a group of events and the determination of a common set of station corrections. We added the "collapsing" method to the JHD results to further consolidate the hypocenters. This was followed by a multiplet analysis for identifying microearthquakes with similar waveforms. We found 7463 events whose seismograms correlated with a correlation coefficient of 0.8 or higher, most of which were doublets. For the relative location of the correlated events, we computed the delay in travel-time by wavelet analysis. We found that multiplets were located on small planes with lengths of a hundred to several hundred meters striking mostly along N150°E. Comparing the distribution of seismicity with fluid outflows during the fluid injection, we observed that majority of events were concentrated along the newly created fractures.

1. Introduction

The European Hot Dry Rock research site is situated about 50 km north of Strasbourg, France in the Northern flank of the Rhine Graben, which is part of the Western European rift system (Figure 1). This graben consists of a granite basement that is covered by sedimentary layers approximately 1400 m thick. The most interesting feature of this site is the anomalous geothermal gradient. The temperature gradient is about 10.5°C/100 m for the first 900 m. It decreases to 1.5°C/100 m below this zone and reaches a temperature of about 200°C at 5000 m deep [Schellschmidt and Schultz, 1991]. The Hot Dry Rock (HDR) or Enhanced Geothermal System (EGS) concept consists of extracting heat energy from the ground by circulating water through fractures between boreholes at great depth (several kilometers). Baria et al. [2004] gives a brief summary of the various stages of the development of this technology at Soultz since 1987.

In order to create a fracture network, massive hydraulic fracturing experiments were carried out at the Soultz Geothermal site. This operation induced a large number of microseismic events, typically more than one hundred events per hour. The location of these microearthquakes allows for the determination of the extent of the stimulated zone and the fracture network [Block et al., 1994; Phillips et al., 1997; Li et al., 1998; Fehler et al., 2001].

In 2003, the two week long hydraulic fracturing experiment generated around 90,000 microearthquakes. Of these, 21,000 events were located individually with a grid search algorithm. However, in our case, the uncertainty of the absolute locations of the individual events was on the order of 70 m [Dyer, 2004]. In order to improve the location and better characterize the fractures we undertook several steps. First was the Joint

Hypocenter Determination (JHD) [Pujol, 1988, 2000], which simultaneously locates a group of events and determines a common set of station corrections. The second step was to combine the Joint Hypocenter Determination technique with collapsing [Jones and Stewart, 1997; Fehler et al., 2000]. The collapsing technique consists of moving events within a confidence interval in a direction toward the center of mass of the events within this interval. The third approach was the use of multiplet analysis. In this approach, cross-correlation of waveforms is used to identify similar waveforms.

Correlated events are called multiplets and are considered to be close to each other, most likely on the same fracture [Moriya, 2002]. As a consequence, they can be used to determine the geometry of fractures [Tezuka and Nitsuma, 1997; Gaucher et al, 1998]. Got et al. [1994] applied this to events from the Kilauea Volcano. Moriya et al. [1994] estimated the direction of fracture growth associated with lost circulation during well drilling at Kakkonda geothermal field in Japan. Fremont and Malone [1987] studied multiplets that occurred at Mount St Helens and interpreted them as repeated slip events within a small volume due to high strain rates around the magma conduit. A great benefit of multiplet analysis is the high precision it provides. Moriya et al. [2003] used multiplet-clustering analysis to estimate the locations of multiplet clusters and to identify fracture systems with high resolution and accuracy. They suggest that they can obtain a relative location with1 an uncertainty of about 5 m.

Precise relative locations can provide new insights into fault structures. Hauksson and Shearer [2005] and Shearer et al. [2005] relocated a great number of microearthquakes in Southern California with waveform cross-correlation. They found that the relocated events are more clustered and are aligned in planar features suggestive of faults. Waldhauser and Ellsworth [2002] relocated earthquakes along the Hayward Fault in California using the Double-Difference method. The relocated seismicity reveals a narrow fault zone along the Hayward trend. Waldhauser and Richards [2004] and Yang et al. [2005] applied the Double-Difference technique to earthquakes that occurred in Central-Western China. They imaged fault structures that are correlated to the tectonic structure of major fault systems expressed at the surface. Rubin et al. [1999] used a multiplet analysis on large numbers of microearthquakes from faults in California and Hawaii, which shows that the locations define highly concentrated streaks that are aligned in the direction of fault slip.

In the following, we show our relocation effort using the Joint Hypocenter Determination coupled with collapsing and the multiplet relative location. Using these techniques, we achieve much better accuracy than locating the events individually.

2. Seismicity Associated with Hydraulic Fracturing at Soultz

In one phase of hydraulic fracturing at Soultz (summer 2003), a total of 34,000 m^3 of fluid (Figure 2b) was injected between 4400 m and 5091 m depths to stimulate the GPK-3 well, one of the three wells in the cluster (Figure 3). The objective was to enhance the permeability of the deepest section of granite. The stimulation was initiated by injecting saturated brine at a flow rate corresponding to a pressure above that required for the onset of fracturing. Having started the stimulation process using this heavy injection fluid, the stimulation continued with the injection of fresh water. Injection rates were as high as 93 l/s (Figure 2b).

A five-station downhole seismic monitoring system was set up and operated during the injection and after the shut-in of the wells (Figure 3b). Geophones were deployed in wells GPK-1 and EPS-1 (3499 m and 2017 m depth, respectively) and 4-axis accelerometers in the observation wells 4601, 4550 and OPS-4, at depths 1539 m, 1482 m and 1485 m depth, respectively (Figure 3). All these seismic sensors were installed below the granite–sediment interface in order to avoid the effects of attenuation and scattering in sedimentary layers. The seismic network was a triggered system with a sampling rate of 2000 Hz.

During the stimulation test, 90,648 triggers were recorded by the down-hole network. Of these, 21,634 events that were recorded by at least four stations were located individually (Figure 3). The seismic activity was high throughout the entire experiment with an average of 300 events per hour (Figure 2a). A maximum of 580 events per hour were observed just after the flow rate test of 93 l/s (Figure 2). During this test, the seismic activity was well-correlated with the flow rates: each time the flow rate was increased the number of events per hour increased. After the shut-in of the well GPK-3, the number of events per hour decreased with time. But continuing seismic activity was observed for the duration of the experiment. Three largest events, of local magnitude ranging between 2.7 and 2.9, occurred during the shut-in. An increase in the seismic activity was observed before each of these events. A venting test (i.e. withdrawal of fluid) in the well GPK2 was conducted in order to decrease the over-pressure within the stimulated zone and to reduce the seismic activity.

At the end of the experiment, the seismicity cloud had approximate dimensions of 1.5 km by 2.5 km by 1.5 km, striking N30°W (Figure 3). This trend was consistent with the orientation of the major horizontal stress direction, which is N165°E [Dezayes, 2005]. The moment magnitudes of these microearthquakes approximately ranged between Mw = -2 and 2.9.

With the 2000 Hz sampling, we could observe signals at high frequency range. Figure 4 shows a typical displacement spectrum. The dominant peak at 100 Hz has a high signal to noise ratio. Because of the high frequencies, we could determine phase arrival times with high precision and locate events with good accuracy.

3. Hypocenter Determination

Hypocenters shown in Figure 3 are those located individually. We relocated the seismic events with a Joint Hypocenter Determination (JHD) technique [Pujol, 1988]. The basic aspect of the technique is to jointly locate a number of events and at the same time to determine a correction term for each of the stations. Starting with the initial catalogue composed of 21,000 events, we ended up with 13,000 microearthquakes with RMS errors less than 0.02s. As the next step, we applied a collapsing technique to highlight linear features in the cloud of earthquakes [Jones and Stewart, 1997]. Figure 5 shows the results after relocation with JHD and collapsing. As compared to the initial location shown in Figure 3, the hypocenters in Figure 5 show several seismic zones (clusters) both in depth cross-section and map view. There is a prominent N-S trending cluster intersecting the well at around 4800 m depth and another cluster of similar trend intersecting the well at 4500 m depth. The last zone is where the largest induced earthquake (M2.9) occurred after the shut-in (indicated by a circle in Figure 5). Smaller, NNW and SSW clusters are also observed.

Figure 6 shows three different slices of relocated and collapsed seismic events at three depth intervals: (a) between 4450 and 4550 m, (b) between 4650 and 4750 m and (c) between 4800 and 5000 m depth. These slices are at depths where major increases in flow rate were observed during fluid injection. NW and NNW trending clusters are prevalent at the two shallower depth section, and NS and SSW trends in the deepest section. It is reasonable to assume that the trends shown are related to the geometry of the fractures at these depths.

4. Multiplet Analysis

Analysis of seismicity catalogs and seismic waveforms in different parts of the world show that in each region there are clusters of events whose waveforms are almost identical (e.g. natural earthquakes in California, [Waldhauser and Ellsworth, 2002, Shearer et al., 2005] ; earthquakes associated with a volcanic activity, [Got et al., 1994]; induced microearthquakes in geothermal areas, [Moriya et al., 2003]). These events are called multiplets. Because of the strong similarity of the waveforms the hypocenters of the multiplets must be very close to each other.

We applied multiplet analysis to the Soultz data recorded during the stimulation in 2003. The analysis consisted of three steps: 1) find the multiplets and classify them into clusters of similar waveforms; 2) calculate the delay times between a master event and the other earthquakes of the cluster (slave events); 3) relocate each slave event relative to its master event.

4.1. Identification of the Multiplets

We define the multiplet as being a group of seismic events whose P and S onsets and waveforms exhibit strong similarity i.e. characterized by a high cross correlation coefficient [Moriya et al, 2002]. Figure 7 shows the waveforms of five events of one multiplet. Identifying these involves cross-correlation of each seismogram with all other seismograms. We performed the multiplet detection on the P wave train of one of the sensors only, to save time. We selected 133 ms of the waveform starting 5 ms before the P arrival time on the vertical component of the geophone in well EPS1 (at 2017 m depth). We chose this sensor because of its high signal/noise ratio. We did the correlation in frequency domain and for the combination of all the events separated by a distance of 300 m or less. If a(t) and b(t) are the windowed finite data of two seismic signals in the time domain and A(f) and B(f) are their Fourier transforms, respectively the spectral density functions [Moriya, 1994] are

$$S_{ab}(f) = A(f)B(f)^{*},\ S_{aa}(f) = A(f)A(f)^{*},\ S_{bb}(f) = B(f)B(f)^{*} \quad (1)$$

where $S_{aa}(f)$ and $S_{bb}(f)$ are the power spectra and $S_{ab}(f)$ is the cross-spectrum. The asterisks denote the complex conjugate. From these, we can deduce the coherency as

$$Coh^{2}(f) = \frac{|S_{ab}(f)|^{2}}{S_{aa}(f)S_{bb}(f)} \quad (2)$$

For the identification of the multiplets, we averaged the coherency between 60 and 190 Hz where the energy of the events is maximal (Figure 4). Note that, even though multiplets were identified through the P-wave correlations, the displayed seismograms show perfect similarity of S-waves and of the complete seismograms (Figure 7).

We selected all the pairs having a coherency higher than 0.8 and created "sensu stricto" multiplets [Got et al, 1994], as a set in which each element has to be coherent with all other elements of the multiplet. We found 7463 events that were part of the multiplet catalog, representing 35% of the original catalog. The majority of the multiplets are doublets and triplets. The number of multiplets as a function of time is similar to the time history of the total number of events, though the proportion is higher at the beginning of the stimulation (Figure 2a). Note that between May 31 and June 2, the sensor in well 4601 was malfunctioning and the events in that time period were not located. The maximum number of events in a cluster was found to be 24. Figure 8 shows the intervals in hours and minutes (inset) between two consecutive events of a multiplet. Most of the intervals are less than one hour, implying that each cluster was generated by a short seismic burst.

4.2. Time Delay Calculation using Wavelet Analysis

To locate events relative to each other, we decided to use P and S-wave arrivals in the multiplet analysis [Moriya et al., 1994]. This requires a set of time delays computed for each doublet in the multiplet. The doublet is composed of the master event and another event of the cluster called the slave event. The master event is chosen as the event with clear P and S arrivals and a high signal/noise ratio.

Time frequency representation is commonly used to compute the time delay in seismology. However, its resolution is limited by the length of the window used in the Windowed Fourier transform. Therefore, we decided to use a wavelet analysis [Strang and Nguyen, 1996; Antoine et al., 2004] to calculate the time delay between two events of a doublet. A number of studies have shown the ability of wavelets in seismic applications [Soma et al., 2000; Kane et al., 2002; Sze, 2005; Sinha et al., 2005]. Indeed, it is well-suited to analyze time series that are non-stationary [Foufoula-Georgiou and Kumar, 1995; Torrence and Compo, 1998], which is the case with our seismic traces. The advantage of using the wavelet transform is that it has the ability to adapt with the frequency window of the signal. The analysis we used here is called the continuous wavelet transform [Daubechies, 1992; Mallat, 1999; Sinha et al., 2005] and evolves the convolution between the signal and a wavelet that dilates to produce different frequency ranges. The signal is then decomposed into a series of basis functions of finite length consisting of dilated and translated versions of a mother wavelet. This process is similar to Fourier analysis, where the mother wavelet is analogous to the sine wave, and the basis functions in Fourier decomposition are sine waves of various amplitude, phase, and frequency variations of the mother sine wave [Gurley and Kareem, 1999].

We used a Morlet wavelet as a mother wavelet because of its similarity with our time series. It is defined as [Goupillaud et al., 1984]:

$$\psi(t/a) = \frac{1}{\sqrt{a}} \exp\left(i.m.\frac{t}{a}\right).\exp\left(-\frac{(t/a)^2}{2}\right) \quad (3)$$

where m, the wavenumber is taken equal to $\pi.\sqrt{\frac{2}{\log(2)}}$, a is the scaling parameter and t is the time. The Morlet wavelet in eq. (3) is the product of a complex exponential and a Gaussian envelope, where ψ is the wavelet value at non-dimensional time (t/a). The continuous wavelet transform is the inner product (convolution) of the wavelet function with our time series. In our analysis, the wavelet was convolved with the seismic waveform for frequencies between 50 and 200 Hz. An example is shown in Figure 9 where the entire seismic waveforms of each event of a doublet (Figure 9a, c) are represented with the modulus of their continuous wavelet transforms (Figure 9b, d). We can clearly see a strong increase of the modulus of the wavelet transform when the P and S-wave trains arrive (in white at around 80 and 500 ms).

Time delay calculation was done in two steps: first, we computed the wavelet transform of the P wave trains and calculated the P wave time delay using the phases of the two wavelet transforms. Then, we used this delay to align the two traces at the P wave and repeated the same procedure for the S wave train. This later delay is used to relocate the slave event relatively to the master event.

Figure 10a shows the same doublet as in Figure 9 composed of two seismic waveforms recorded in well 4550. For this example, the wavelet analysis is only performed on the P wave train. The wavelet transform of each waveform is calculated on a 210 ms window containing the P arrival. We selected the time t_P and frequency a_P where the modulus of the continuous wavelet transform of the master event is the maximum in order to identify the arrival time of most of the P wave energy, here 90 ms and 118 Hz (Figure 10b). We then calculated the unwrapped phases for each event at that time and frequency (Figure 10c). The difference between phases of the wavelet transforms gives the P wave time delay. Indeed, let f(t) and g(t) be the waveform of the master and slave events, band pass filtered at the frequency a_p, and t_{Pf} and t_{Pg} the P wave arrival time of the master and slave events, respectively. Since these two events are multiplets,

$$g(t_{Pg}) \cong \alpha\, f(t_{Pf}) = f(t_{Pg} + \Delta t) \qquad (4)$$

where α is a real constant related to the ratio of energy of the two events and Δt is the delay between the two P wave arrivals. In the wavelet domain, this relation becomes

$$\varphi_g(t_{Pg}, a_P) \cong \varphi_f(t_{Pf}, a_P) = \varphi_f(t_{Pg} + \Delta t, a_P) = \varphi_f(t_{Pg}, a_P) + \Delta t/(2\pi\, a_P) \qquad (5)$$

where φ_f and φ_g are the phases of the master and slave events, respectively. Therefore, the time delay between the master and the slave events Δt can be obtained from the phases of their wavelet transform. In our example, this delay is used to align the two traces in the P-wave window (Figure 11a). The two traces are perfectly aligned on the P wave train (Figure 11b), whereas a time delay remains on the S wave train (Figure 11c). Using the same wavelet approach, we then computed the time delay of the S wave train that will be used later in the relocation algorithm.

This procedure was done automatically for every waveform pair on four sensors. Of the five stations in the network, only four were usable for the automatic process. The data from sensor in well OPS4 was contaminated by noise due to interference from a transmitter operating at the same frequency as the telemetry. For consistency and accuracy of the delays, each delay was checked manually and recalculated if necessary. 96 clusters (composed of 6 and more events) with a total of 751 events were processed using this procedure.

4.3. Multiplet Event Location

The method used to relocate one event relative to a reference or master event is based on a grid search algorithm. The objective is to find the increments Δx, Δy and Δz to go from the master event to the slave event. In the Soultz case, we consider the medium to be homogeneous, since both the seismic sensors and the events are located in a granitic body. The distance ΔL between two events A and B [Moriya et al., 1994] is

$$\Delta L = \frac{\left(t_S^A - t_P^A\right) - \left(t_S^B - t_P^B\right)}{\frac{1}{V_S} - \frac{1}{V_P}} = \frac{\Delta S - \Delta P}{\frac{1}{V_S} - \frac{1}{V_P}} \quad (6)$$

where $t_s^A, t_P^A, t_s^B, t_P^B$ are the arrival times for the S and the P waves of the events A and B respectively; V_P, V_S are the P and S wave velocities; $\Delta S = t_S^A - t_S^B$ and $\Delta P = t_P^A - t_P^B$. We used constant P and S wave velocities of 5950 m/s and 3440 m/s based on a shot survey data obtained in well GPK1 [Dyer, 1993].

For a given station, these arrival times can be expressed as:

$$t_\alpha^A = t_0^A + \sqrt{\left(x_A - x_{station}\right)^2 + \left(y_A - y_{station}\right)^2 + \left(z_A - z_{station}\right)^2} / V_\alpha \quad (7)$$

where α is either the P or S phase, t_0^A, x_A, y_A and z_A are respectively the origin time, the hypocenter coordinates of the master event A and $x_{station}$, $y_{station}$ and $z_{station}$ are the coordinates of a station.

The P and S arrival times for the slave event B can be approximated by:

$$t_\alpha^B = t_0^B + \sqrt{\left(x_A + \Delta x - x_{station}\right)^2 + \left(y_A + \Delta y - y_{station}\right)^2 + \left(z_A + \Delta z - z_{station}\right)^2} / V_\alpha \quad (8)$$

where α is either the P or S phases, (Δx, Δy, Δz) are the distance between the events in the x-,y- and z- directions and t_0^B the origin time for the slave event B.

Hence, the theoretical difference of the P-S delay between the two microearthquakes A and B is:

$$d_{diff} = \Delta S - \Delta P = t_S^A - t_S^B - \left(t_P^A - t_P^B\right) \quad (9)$$

This difference d_{diff} is also the S wave delay when the traces are aligned on the P wave that we computed previously using the wavelet analysis. Consequently, we have to

minimize the difference between the theoretical and the observed delay. To do so, we used a Root Mean Square error function, defined as:

$$\Delta = \frac{1}{\sqrt{n}} \sum \sqrt{(d - d_{diff})^2} \quad (10)$$

where d is the observed delay time for the doublet at each station and n is the number of observations. We minimized this error function using a grid search algorithm [Sen and Stoffa, 1995].

The location algorithm was applied to 751 seismic events. The location of the master event was chosen to be the average of the initial absolute locations of the other events of the cluster.

4.4. Spatial Distribution

This relocation procedure was done for the 96 clusters and Figure 12 shows the microearthquakes after relocation on vertical and map views. Each color corresponds to a different cluster. The size of the clusters is small; their extent is about 100 m. The fact that the events are so tightly clustered suggests that they represent the progressive failure of a larger patch through stress transfer and/or rising pore pressure [Evans et al., 2005]. The majority of the clusters are located between the wells GPK3 and GPK2 at depths between 4600 and 5300 m (i.e. around the deeper section of the well). This suggests that the stimulated fracture network is denser in the deeper part of the reservoir.

For discussing the significance of seismicity trend, it is important to evaluate the accuracy of the hypocenters. To study the location errors, we performed a Monte-Carlo simulation. We chose an earthquake located within the stimulated area and computed the travel times to each station. We assumed that the time reading errors would have a Gaussian distribution with zero mean and 0.3 ms standard deviation. We drew 500 picking errors from a Gaussian distribution of 0.3 ms standard deviation and ran the location algorithm 500 times. The histograms in Figure 13 show the error of location in each direction. We fitted Gaussian functions to each error distribution and found that the standard deviation of the error is 10 meters in x, 8.5 meters in y and 4 meters in z. These provide a measure of accuracy for the hypocenters shown in Figure 12.

In order to evaluate the shape of the clusters, we performed a principal component analysis and deduced the degree of planarity for each group of events. To do so, we constructed a covariance matrix composed of the locations of the events (x, y, z), defined as

$$C = \begin{bmatrix} xx & xy & xz \\ yx & yy & yz \\ zx & zy & zz \end{bmatrix} \quad (11)$$

The degree of planarity can be expressed by

$$P = 1 - \left(\frac{2\lambda_3}{\lambda_1 + \lambda_2} \right)^n \quad (12)$$

Where $\lambda_1 \geq \lambda_2 \geq \lambda_3$ are the eigenvalues of the covariance matrix C and n is taken to be 0.75 [Sze, 2005]. The planarity is equal to 1 when the earthquake locations lie perfectly on a

plane. All our clusters have a planarity degree higher than 0.9. Figure 14 shows the azimuths and the plunges of these planes. The majority of the azimuths is around N155°E and the trend is nearly horizontal. The general trend shown in Figures 5 and 6 and the azimuth found here are consistent with orientation of the major horizontal stress direction [Dezayes et al., 2005], suggesting that direction of hydraulic fractures is consistent with the regional tectonic stress. Besides, analysis of UBI (Ultrasonic Borehole Imager – Schlumberger) data in the GPK3 well permits the determination of the orientation of fractures. Dezayes et al. [2005] found that the average direction of the fractures is N150°E.

5. Discussion & Conclusions

The analysis of 21,000 microseismic events generated during the hydraulic fracturing in May-June 2003 in Soultz-sous-Forêts, showed several patterns. First, the epicenters are not distributed in a circular pattern around the well. Both JHD and multiplet location results (Figures 5, 6 and 12) show a strong elongation in the NNW direction favored by the regional stress field for fracture growth. Second, the distribution of induced events is not uniform with depth. These suggest that the seismogenic fractures were created at some selected depths. In the GPK3 well, where fluid injection took place, open (uncased) portion of the well was between 4500 m (casing shoe) and 5000 m (TD) depths. The seismicity was between 4000 m and 5500 m (Figure 5). The density of seismic events shows considerable variation as a function of depth. The comparison of depth distribution and the flow logs (Figure 15) conducted in various stages of stimulation in GPK3 well, provide some insights into the fracturing and the density of microseismic events. Distribution of all events located by JHD (Figure 15a) shows a broad and prominent peak at 5000 m depth and a broad minimum centered between 4600 and 4700 m depths. The multiplet locations (Figure 15b) show peaks at about 4500, 4600, 4900 and 5100 m depths, although there are far fewer events in this distribution. The flow logs were obtained in GPK3 well before the stimulation and at different times during the stimulation. These are shown in Figure 15c. The curves are the normalized flow rates. 100 % means that there is no flow from the well into the formation. The flow distribution before the stimulation was indeed dominated by a feature at 4685 m depth with nearly 90% of the production flow reaching the well at this depth [Baumgartner et al., 2005]. This fracture should be large because it intersects the wells GPK2, GPK3 and GPK4, each separated by approximately 500 m from each other [Dezayes et al., 2005]. This zone has also been seen on a UBI (Ultrasonic Borehole Imager – Schlumberger) log as a large fracture zone [Hettkamp et al., 2004]. At the end of the stimulation, three major fluid outlets are observed: the first one (10 %) is at app. 4480 m depth, the second (70%) at app. 4685 m depth and the last one (20%) is at app. 4940 m depth. No peak seismicity is seen around 4685 m depth, natural (pre-existing) fracture could not accumulate stress to generate large amount of seismicity. Among the newly created fractures, the most prominent zone that controls 20 % of the flow at 4940 m depth corresponds to the maximum of seismicity shown in Figure 15b. There is another peak at about 4500m, which may correspond to flow anomaly at 4480 m depth. This demonstrates that the collapsing and multiplet techniques not only locate events more precisely but also characterize events that belong to newly created permeable fractures.

The Joint Hypocenter Determination coupled with collapsing enables us to delineate the seismic zones with a better resolution than individually located events. Thus, the trends of the relocated microearthquakes allow imaging the geometry of the newly created fractures. The multiplet analysis provides a precise relative location (~10 meters). That permits us to characterize further the geometry of fracture planes. We found that the azimuths of the fracture planes determined by multiplets were bunched tightly and consistent with the orientation of the major horizontal stress direction. These two techniques improve the spatial resolution for mapping hydraulic fractures in geothermal, oil/gas reservoirs, as well as in the analysis of induced and natural seismicity.

6. Acknowledgements

This work was supported by the ERL Founding Member Consortium. We would like to acknowledge the funding agencies supporting the Soultz project: Directorate Research of the European Commission, ADEME (France), BMWi (Germany), EEIG Heat Mining.
We want to give many thanks to M. Darnet, M. Benoit, B. Minsley and Y. Sun for suggestions on the manuscript. The authors would like to thank D. Teza, R. Baria, J. Baumgartner, B. Dyer and J. Nicholls for their support.

References

Antoine, J.-P., R. Murenzi, P. Vandergheynst, and S. T. Ali (2004), Two-Dimensional Wavelets and their Relatives, Cambridge University Press, ISBN: 0521624061.

Baria, R., S. Michelet, J. Baumgaertner, B. Dyer, A. Gerard, J. Nicholls, T. Hettkamp, D. Teza, N. Soma, H. Asanuma, J. Garnish, and T. Megel (2004), Microseismic monitoring of the world's largest potential HDR reservoir, Proceedings of the 29th Workshop on. Geothermal Reservoir Engineering, Stanford University, California.

Baumgärtner, J., D. Teza**,** T. Hettkamp**,** G. Homeier, R. Baria, and S. Michelet (2005), Electricity Production from Hot Rocks**,** Proceedings World Geothermal Congress, Antalya, Turkey.

Block, L., C. Cheng, M. Fehler, and W.S. Phillips (1994), Seismic imaging using microearthquakes induced by hydraulic fracturing, *Geophysics*, 59, 102-112.

Daubechies, I. (1992), Ten Lectures on Wavelets, SIAM, Philadelphia, Pa.

Dezayes, C., A. Genter, and G.R. Hooijkaas (2005), Deep-Seated geology and fracture system of the EGS Soultz reservoir (France) based on recent 5km depth boreholes, Proceedings World Geothermal Congress, Antalya, Turkey.

Dyer, B., A. Jupe, R.H. Jones, T. Thomas, J. Willis-Richards, and P. Jaques (1993), Microseismic results from the European HDR geothermal project, Soultz-sous-Forets, Alsace, France – CSMA report no. IR03/24.

Dyer, B. (2004), Soultz GPK3 Stimulation 2003 and GPK3-GPK2 circulation May to July 2003, Seismic Monitoring Report, EEIG05/2004.

Evans, K. F., H. Moriya, H. Niitsuma, R. H. Jones, W. S. Phillips, A. Genter, J. Sausse, R. Jung, and R. Baria (2005), Microseismicity and permeability enhancement of hydrogeologic structures during massive fluid injections into granite at 3 km depth at the Soultz HDR site, *Geophysical Journal International*, 160 (1), 389-412.

Fehler, M., W.S. Phillips, R. Jones, L. House, R. Aster, and C. Rowe (2000), A method for improving relative earthquake locations, *Bulletin of the Seismological Society of America*, 90, 775-780.

Fehler, M., A. Jupe, and H. Asanuma (2001), More than Cloud, New techniques for characterizing reservoir structure using induced seismicity: THE LEADING EDGE, 20, no. 03, 324-330.

Foufoula-Georgiou, E., and P. Kumar, Eds., 1995: Wavelets in Geophysics. Academic Press, 373 pp.

Fremont, M.J., and S. Malone (1987), High precision relative locations of earthqaukes at Mount St. Helens, Washingthon, *Journal of Geophysical Research*, 92, 10,223-10,236.

Gaucher, E., F. Cornet, and P. Bernard (1998), Induced seismicity analysis for structure identification and stress field determination, Paper SPE 47324, Proc. SPE/ISRM, Trondheim, Norway.

Got, J.-L., J. Frechet, and F. Klein (1994), Deep fault plane geometry inferred from multiplet relative relocation beneath the south flank of Kilauea, *Journal of Geophysical Research*, 99, 15,375-15,386.

Goupillaud, P., A. Grossmann, and J. Morlet (1984), Cycle-octave and related transforms in seismic signal analysis, *Geoexploration*, 23, 85-102.

Gurley, K., and Kareem, A (1999), Applications of Wavelet Transforms in Earthquake, Wind, and Ocean Engineering, Engineering Structures, 21, pp. 149-167.

Hauksson, E., and P. Shearer (2005), Southern California hypocenter relocation with waveform cross-correlation, Part 1: Results using the double-difference method, *Bulletin of the Seismological Society of America*, 95, 896-903, doi:10.1785/0120040167.

Hettkamp, T., J. Baumgärtner, R. Baria, A. Gerard, T. Gandy, S. Michelet, and D. Teza (2004), Electricity Production from Hot Rocks, Proceedings of the 29th Workshop on Geothermal Reservoir Engineering, Stanford University, California.

Kane, J., F. J. Herrmann, and N. Toksöz (2002), Wavelet domain geophysical inversion, in Expanded Abstracts, Soc. Expl. Geoph.

Jones, R., and R.C. Stewart (1997), A method for determining significant structures in a cloud of earthquakes, *Journal of Geophysical Research*, 102, 8245-8254.

Li, Y., C. Cheng, and N. Toksöz (1998), Seismic monitoring of the growth of a hydraulic fracture zone at Fenton Hill, New Mexico, *Geophysics*, 63, 120-131.

Mallat, S. (1999), A Wavelet Tour of Signal Processing, Academic, San Diego, 2nd edition.

Moriya, H., K. Nagano, and H. Nitsuma (1994), Precise source location of AE doublets by spectral matrix analysis of triaxial hodogram, *Geophysics*, 59, 36-45.

Moriya, H., K. Nakazato, H. Nitsuma, and R. Baria (2002), Detailed fracture system of the Soultz-sous-Forêts HDR field evaluated using microseismic multiplet analysis, *Pure appl. Geophys*., 159, 517-541.

Moriya, H., H. Nitsuma, and R. Baria (2003), Multiplet-Clustering Analysis reveals structural details within the seismic cloud at the Soultz Geothermal Field, France, *Bulletin of the Seismological Society of America*, 93, 1606-1620.

Phillips, W.S., L. House, and M. Fehler (1997), Detailed joint structure in a geothermal reservoir from studies of induced microearthquake clusters, *Journal of Geophysical Research*, 102, 11745-11763.

Pujol, J. (1988), Comments on the joint determination of hypocenters and station corrections, *Bulletin of the Seismological Society of America,* 78**,** 1179-1189.

Pujol, J. (2000), Joint event location - The JHD technique and applications to data from local seismic networks. In "Advances in seismic event location", Thurber C., and N. Rabinowitz , 163-204, Eds. Kluwer Academic Publishers.

Rubin, A.M., D. Gillard, and J.-L. Got (1999), Streaks of microearthquakes along creeping faults, *Nature*, 400, 635-641.

Schellschmidt R, and R. Schulz (1991), Hydrothermic studies in the Hot Dry Rock Project at Soultz-sous-Forêts, Geothermal Science and Technology, vol. 3(1-4), pp. 217-238, Bresee (Ed), Gordon and Breach Science Publishers.

Sen, M.K., and P.L. Stoffa (1995), global optimization methods in geophysical inversion, 294 pages, Elsevier Publication.

Shearer, P., E. Hauksson, and G. Lin (2005), Southern California hypocenter relocation with waveform cross-correlation, Part 2: Results using source-specific station terms

and cluster analysis, *Bulletin of the Seismological Society of America*, 95, 904-915, doi:10.1785/0120040168.

Sinha, S., Routh, P.S., Anno, P. D., and Castagna, J. (2005), Time Frequency attribute of seismic data using continuous wavelet transform, *Geophysics*, 70, p19-25.

Soma, N., H. Niitsuma, and R. Baria (2000), Reflection Imaging of HDR Reservoir at Soultz by Means of the AE Reflection Method, Proceedings World Geothermal Congress 2000, Kyushu - Tohoku, Japan.

Strang, G., and T. Nguyen (1996), Wavelets and Filter Banks, Wellesley-Cambridge Press, ISBN 09614088 71.

Sze, E. (2005), Induced seismicity analysis for reservoir characterization at a petroleum field in Oman, PhD thesis, Massachusetts Institute of Technology.

Tezuka, K., and H. Nitsuma (1997), Integrated interpretation of microseismic clusters and fracture system in a hot dry rock artificial reservoir, SEG 67th Annual Meeting Expanded Abstracts, Dallas, USA, 657-660.

Torrence, C., and G. Compo (1998), A Practical Guide to Wavelet Analysis, *Bulletin of the American Meteorological Society*, 79, 61-78.

Yang, Z.X., F. Waldhauser, Y.T. Chen & P.G. Richards (2005), Double-difference relocation of earthquakes in central-western China, 1992–1999, *Journal of Seismology*, 9, 241–264.

Waldhauser F., and W. L. Ellsworth (2002), Fault structure and mechanics of the Hayward Fault, California, from double-difference earthquake locations, *Journal of Geophysical Research*, 107, doi:10.1029/2000JB000084.

Waldhauser F., and P.G. Richards (2004), Reference events for regional seismic phases at IMS stations in China, *Bulletin of the Seismological Society of America*, 94, 2265-2279.

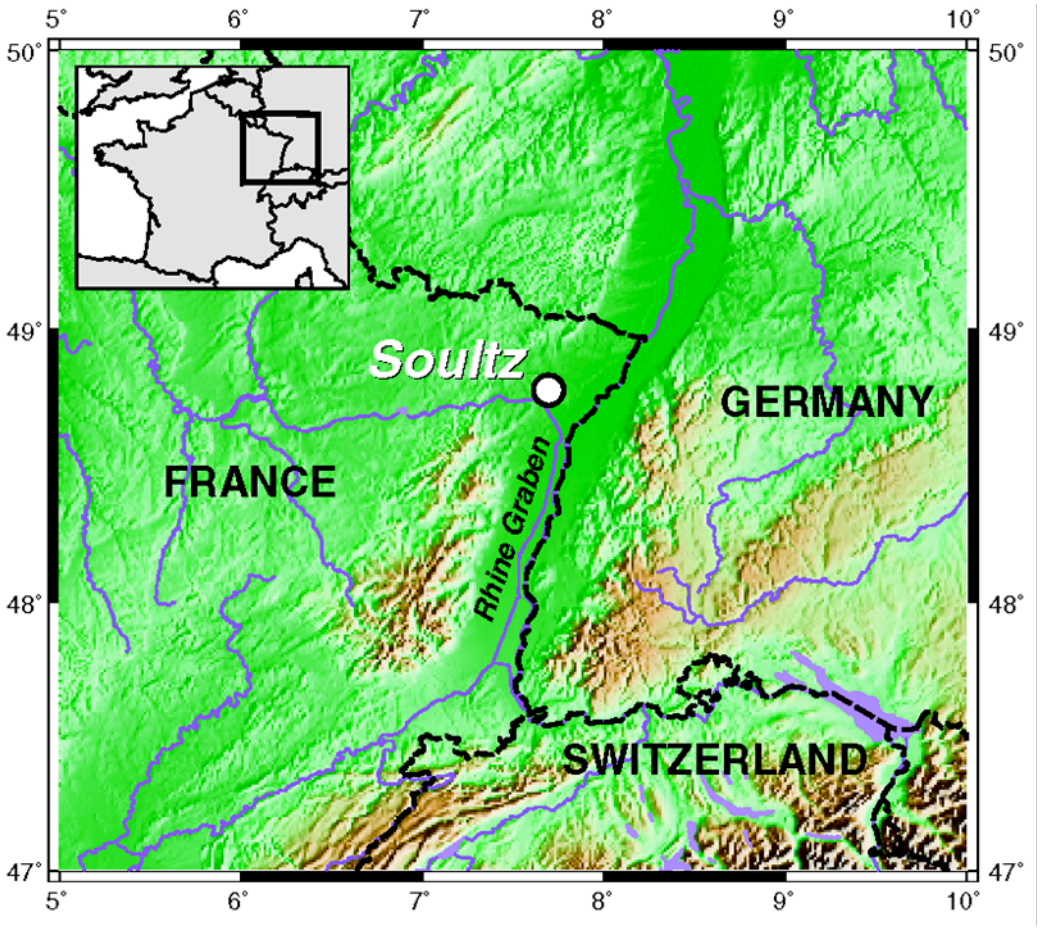

Figure 1. The location of the Hot Dry Rock geothermal site in Soultz-sous-Forêts, France.

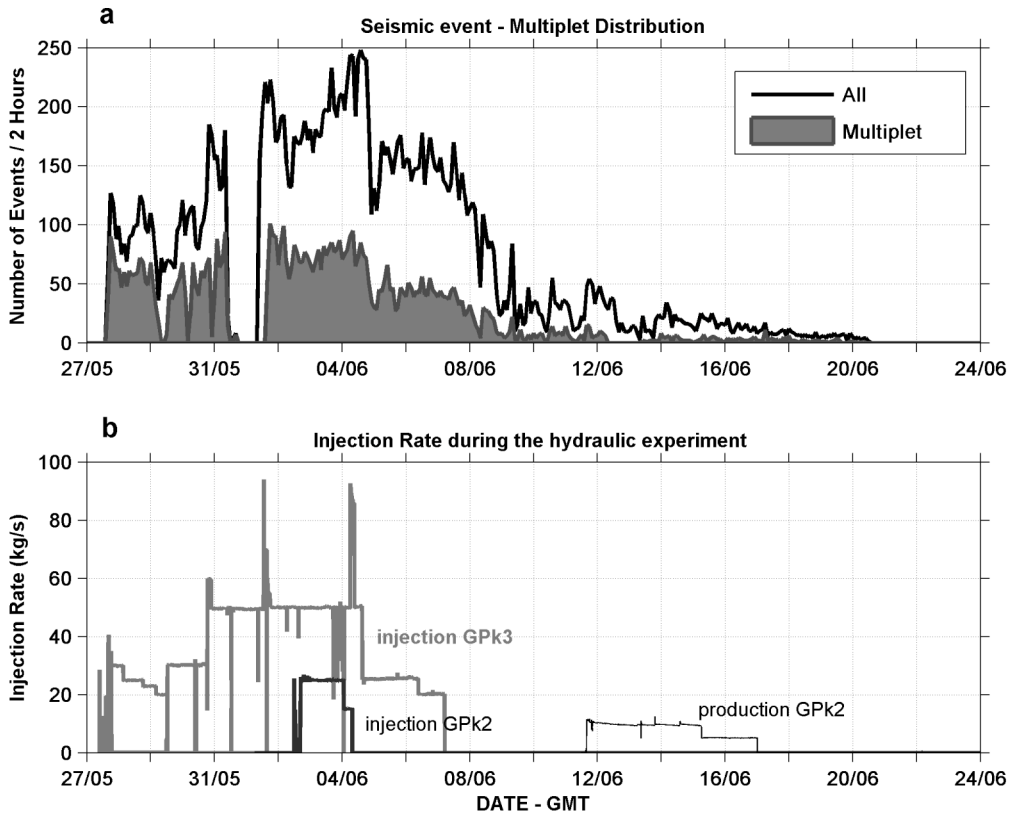

Figure 2. (a) Number of microseismic events (black line) and multiplets (gray area) per two hours as a function of time. There is a gap in the seismic rate the 1st of June due to a malfunction of seismic sensors. The number of multiplets per 2 hours follows the total number of events per 2 hours, though the proportion is the highest at the beginning of the experiment. (b) Injection and production rates as a function of time during the hydraulic experiment. The injection rates in the GPK3 and GPK2 wells are in gray and black respectively; the production in the GPK2 well is in dark gray as indicated in the Figure. The hydro-fracturing experiment started with fluid injected in GPK3; followed by a double injection (injection the 2 wells at the same time), and finally a high injection rate (93l/s) and a stepped decrease rate ended the stimulation. Four days after the shut-in, a production test was performed. A good correlation between the seismic rate and the injection rate is observed.

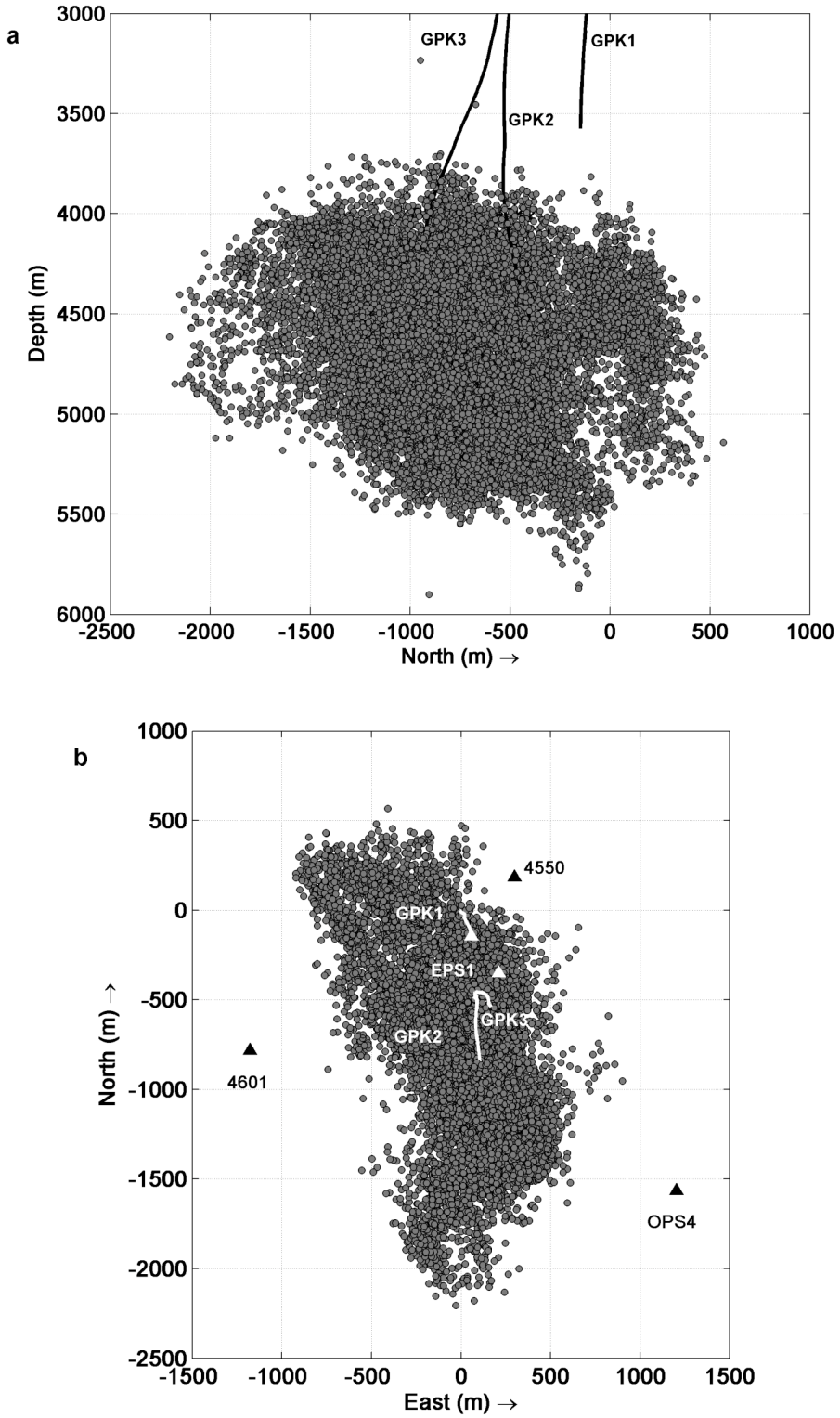

Figure 3. (a) Vertical view and (b) map view of the seismicity associated with the stimulation in 2003 - the downhole seismic stations are represented by triangles on the map view. More than 21,000 events were located and they are the starting point for our Joint Hypocenter Determination and multiplet analysis.

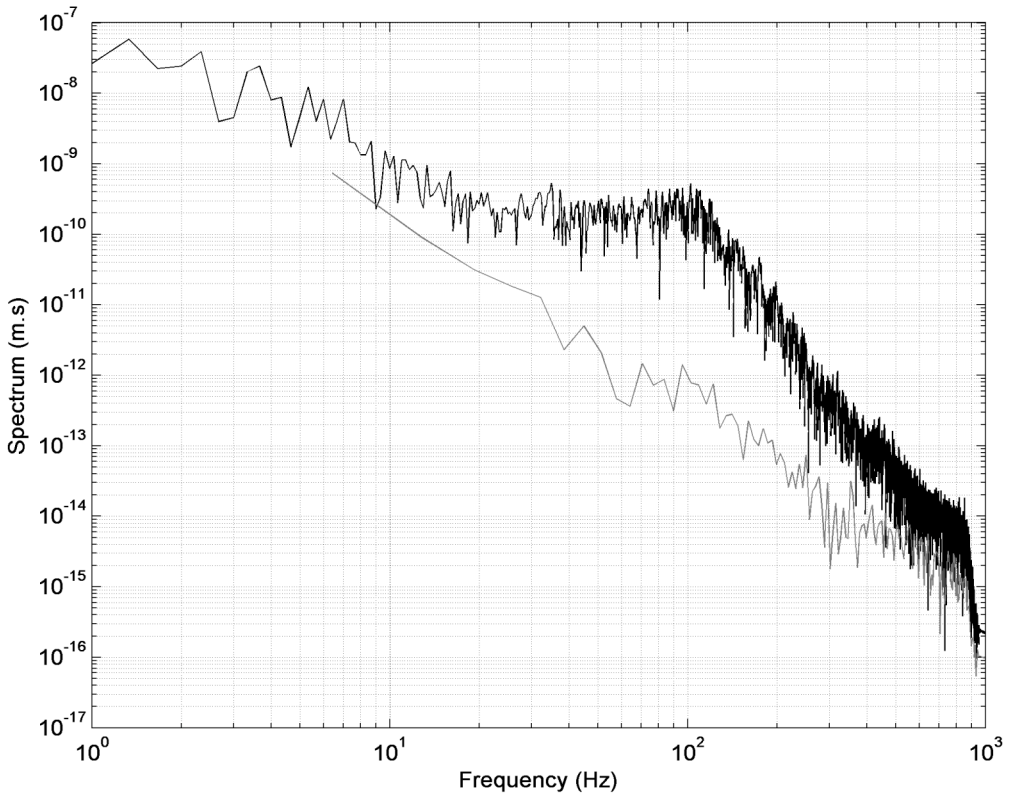

Figure 4. Example of a displacement spectrum (in black) of a typical waveform showing that the dominant frequency is around 100 Hz. The noise spectrum is in grey.

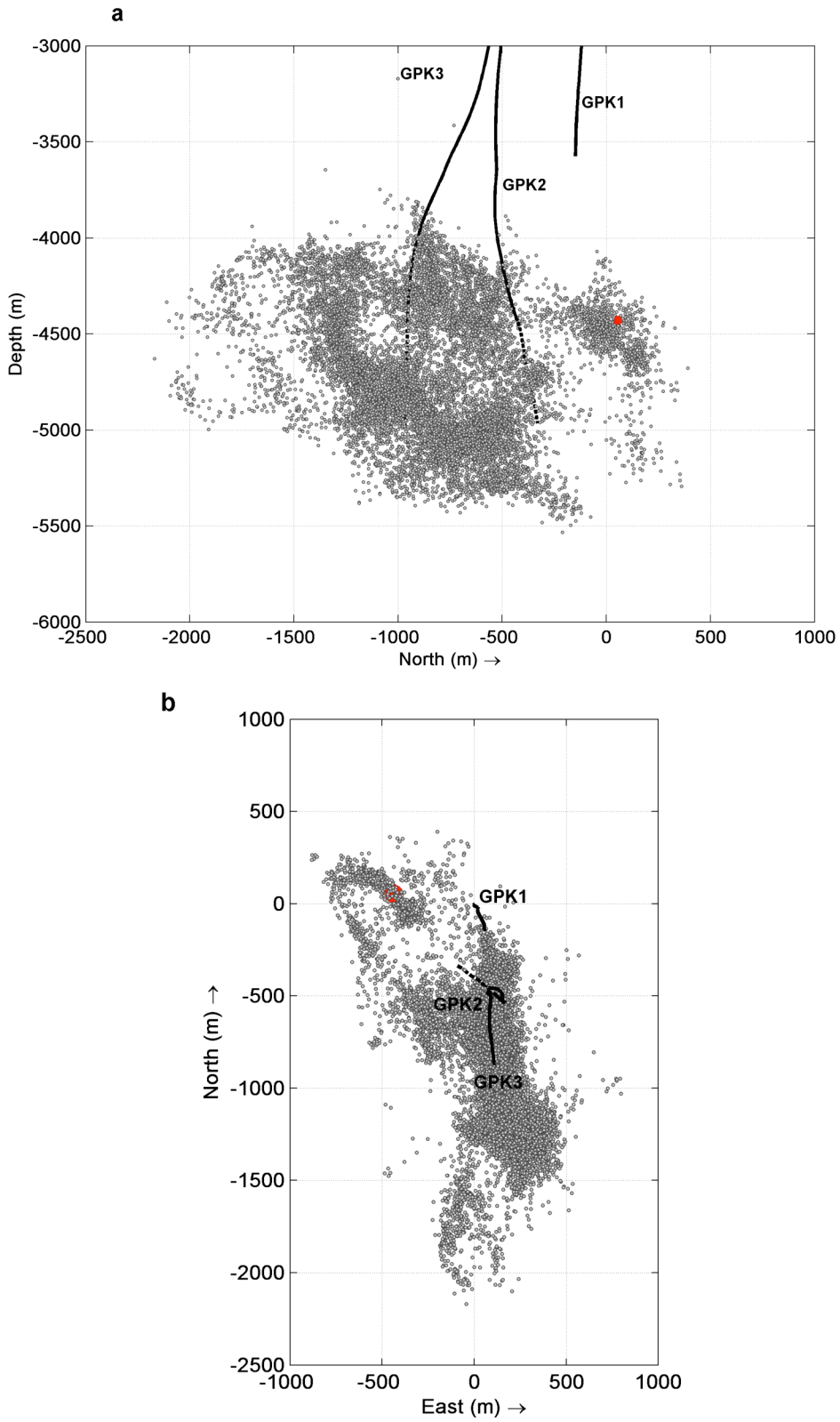

Figure 5. (a) Vertical view and (b) top view of the seismic events relocated with the Joint Hypocenter Determination and collapsed. The M2.9 earthquake is represented by a red circle.

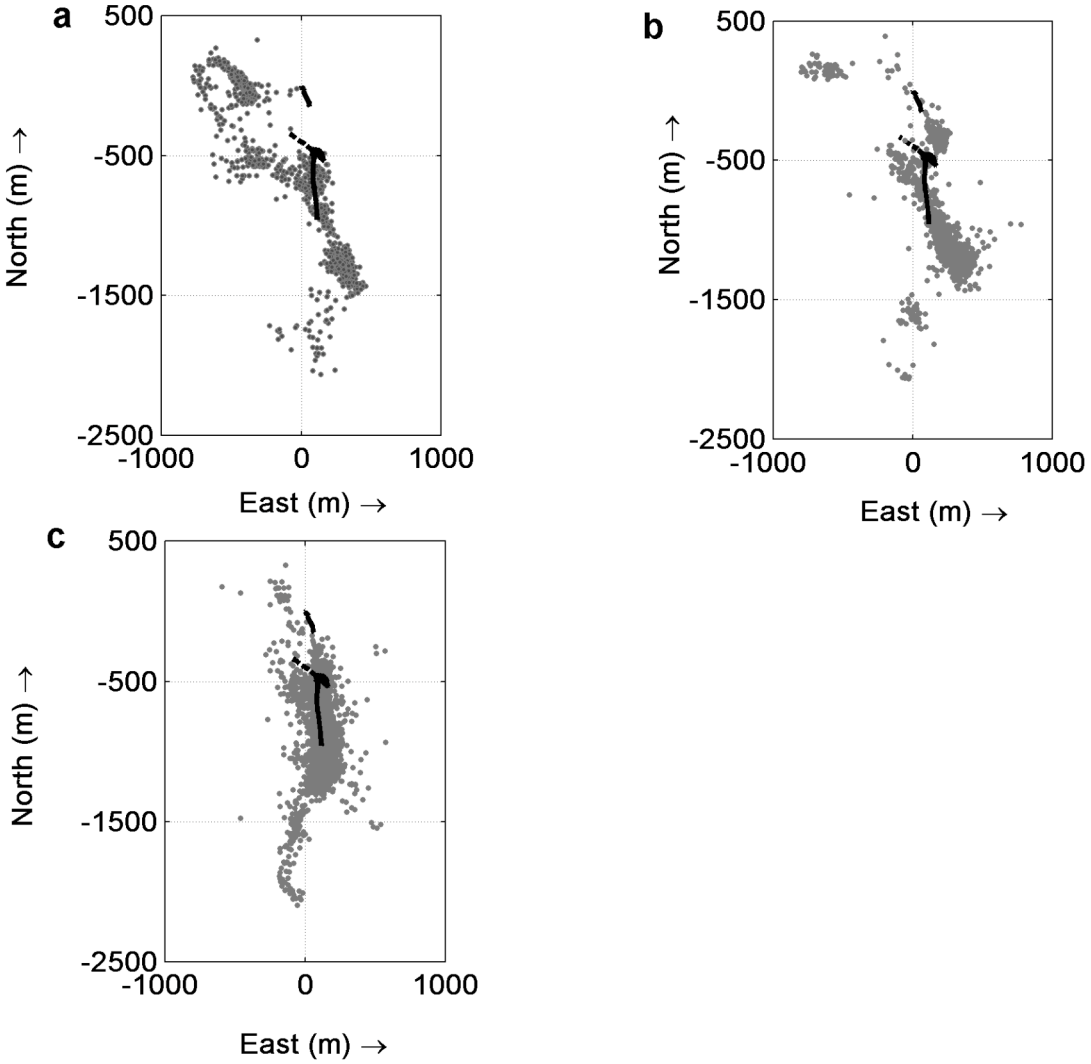

Figure 6. The seismic events relocated with the Joint Hypocenter Determination and collapsing at three depth intervals: (a) between 4450 and 4550 m, (b) between 4650 and 4750 m and (c) between 4800 and 5000 m depth.

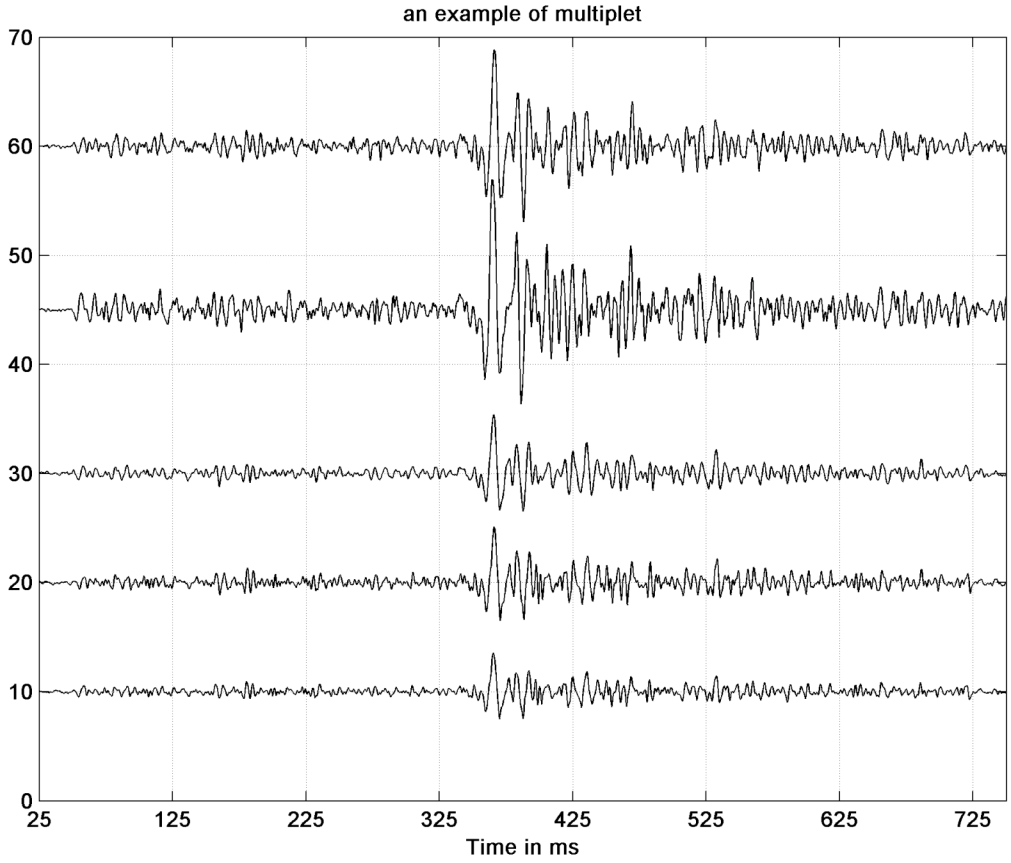

Figure 7. Seismic waveforms - example of a multiplet composed of 5 microearthquakes. The waveforms show a high similarity around the P-wave and the S-wave arrivals.

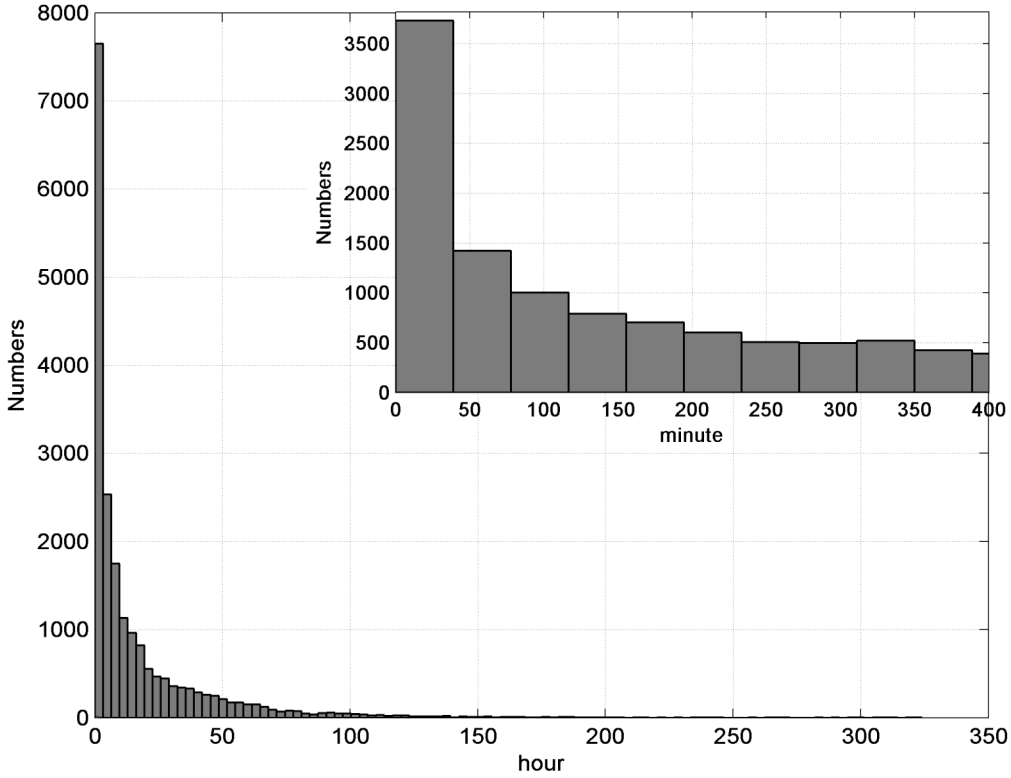

Figure 8. Distribution of the time lag in hours and in minutes (inset) between two consecutive events of a cluster. The inset shows that the majority of the consecutive events are separated in time by less than one hour.

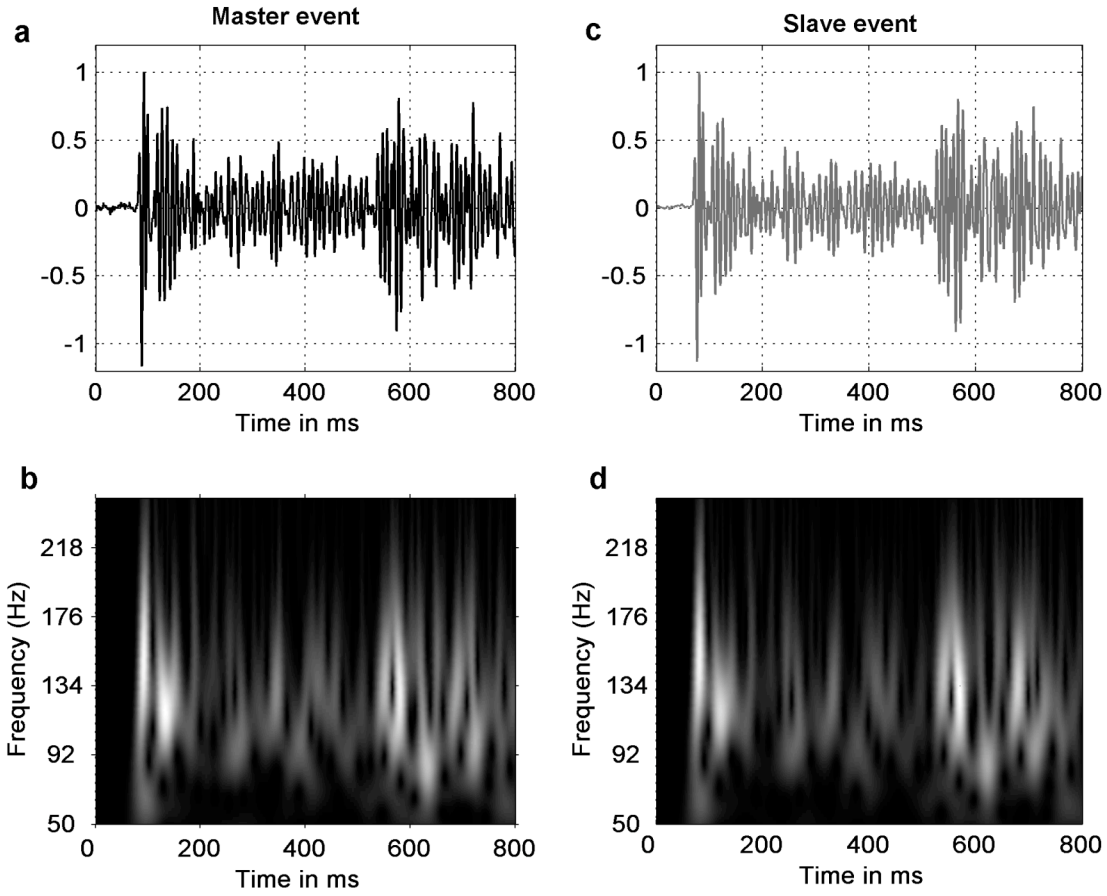

Figure 9. (a) Waveform of a master event and (b) its wavelet transform modulus; (c) Waveform of its slave event and (d) its wavelet transform modulus. The scale in gray is the maximum when the color is white. We can see a strong increase of the modulus of the wavelet transform when the P and S-wave trains arrive (in white at around 80 and 500 ms).

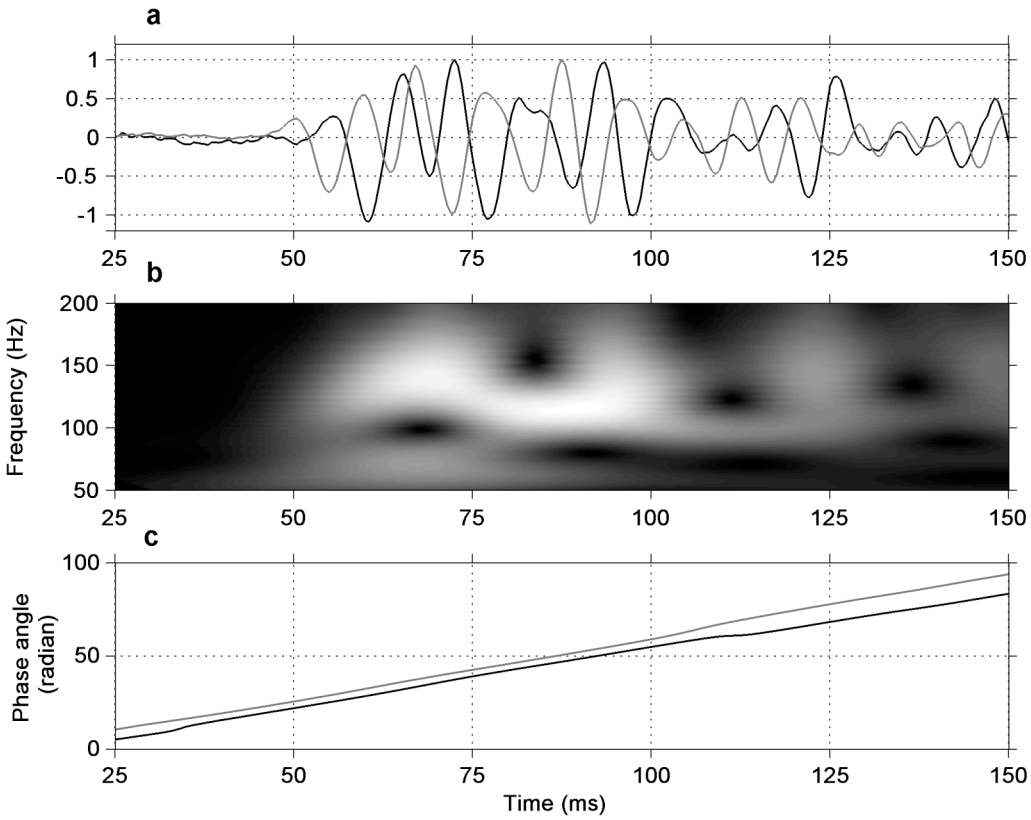

Figure 10. (a) P-wave train of the master event (black line) and its slave event (gray line), (b) the modulus of the wavelet transform of the master event and (c) the unwrapped phase angles of the master event and its slave event. In (a) and (c), the master event is in black and the slave event in gray. The goal is to find the time delay between the two traces. To do so, the wavelet transform of each waveform is calculated on a 210 ms window containing the P arrival. We then selected the time and frequency where the modulus of wavelet transform of the master event (b) is the maximum to identify the arrival time of most of the P wave energy, here 90ms and 118Hz. We then calculated the unwrapped phases for each event at that time and frequency (c). If the P waves of the two events are not in phase, the phases of the wavelet transform show a constant time shift that is equal to the P wave time delay. In order to calculate this time delay automatically, we interpolated in time the phases of the wavelet transform around its maximum (80-100ms in our example) and performed a linear regression. This delay is then used to align the two traces in the P-wave window as shown in Figure 11.

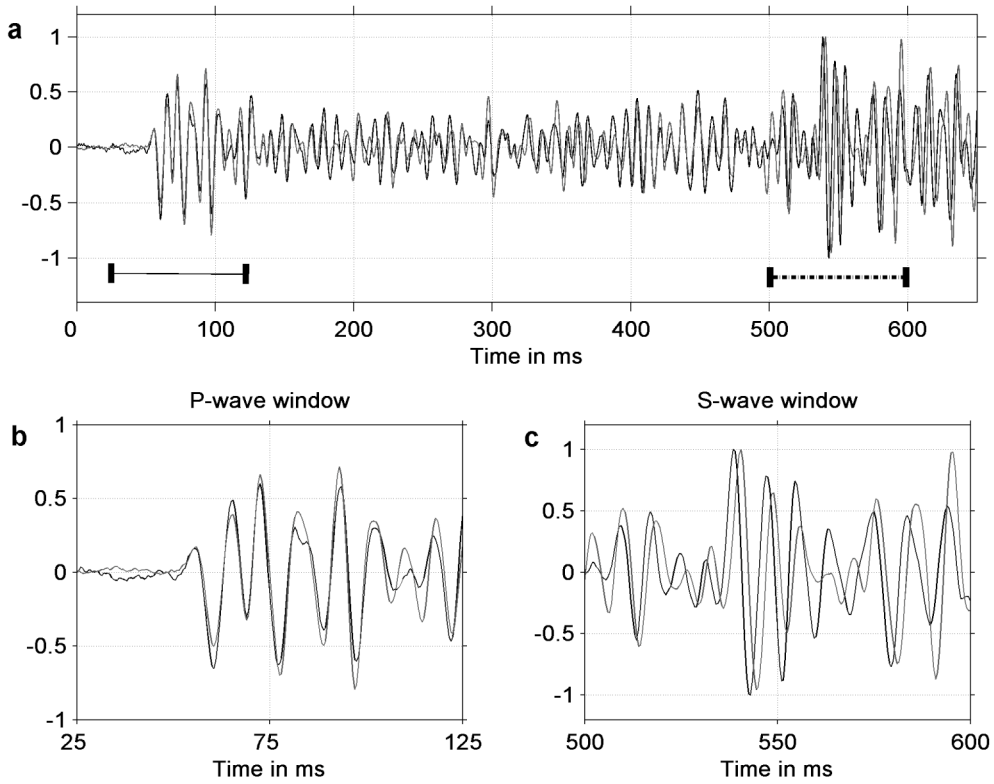

Figure 11. (a) Aligned waveforms of the master event (black line) and the slave event (grey line) after adjusting the P-wave time delay by wavelet analysis. (b) Zoom of the P-wave train after alignment as pointed by the black line from 25 to 125 ms in Figure 11a. (c) Zoom of the S-wave train as indicated by the dashed black line from 500 to 600 ms in Figure 11a. The two traces are perfectly aligned on the P wave train (b), whereas a time delay is seen on the S wave train (c). This time delay is computed in the same way as on Figure 10 and will be the input to the grid search relocation algorithm.

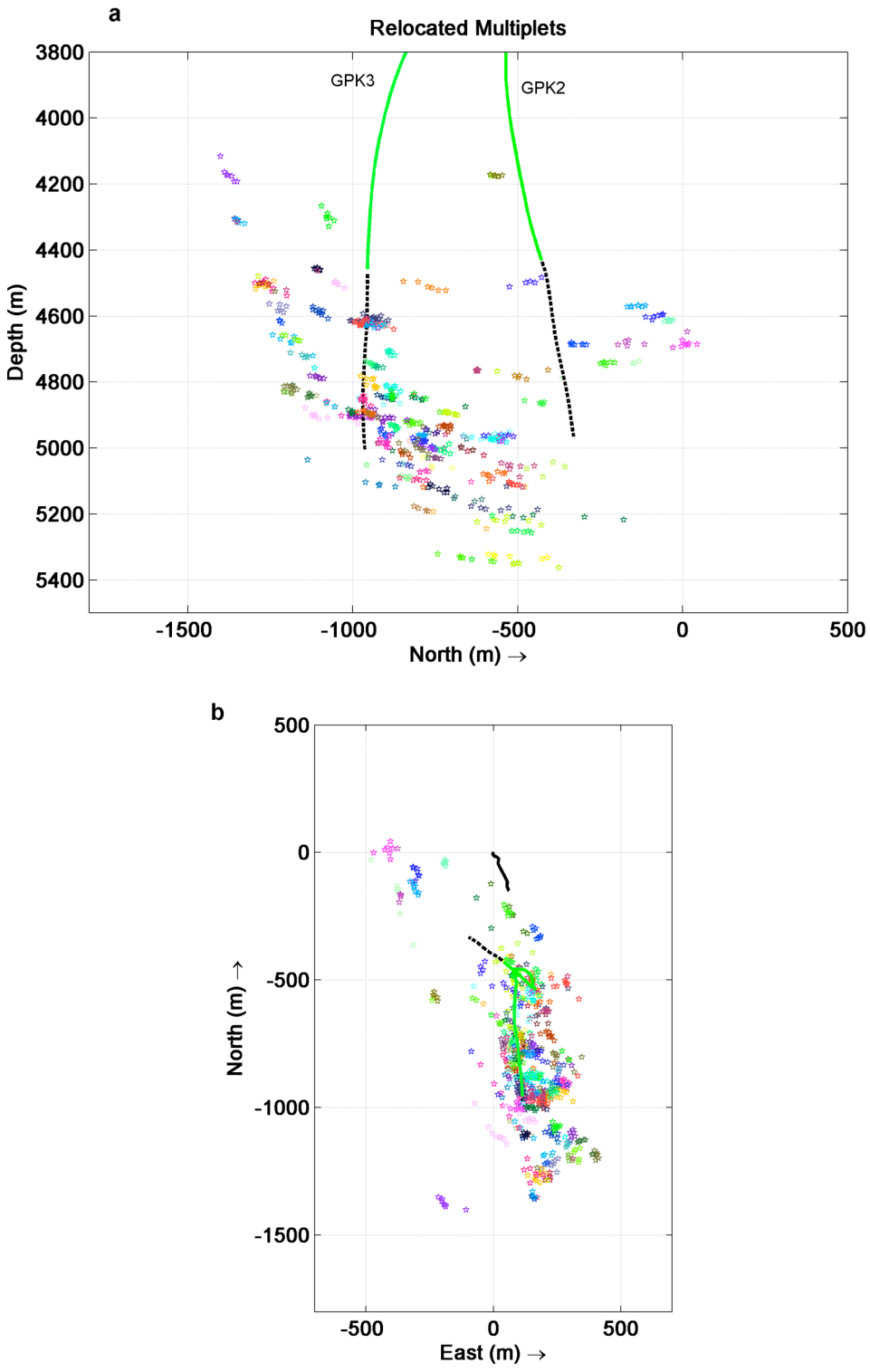

Figure 12. Relocated clusters in (a) a vertical view and (b) in a map view. Each cluster is represented by a different color. The size of the clusters is small, events are found to be really close to each other: their extent is less than 100 m in general.

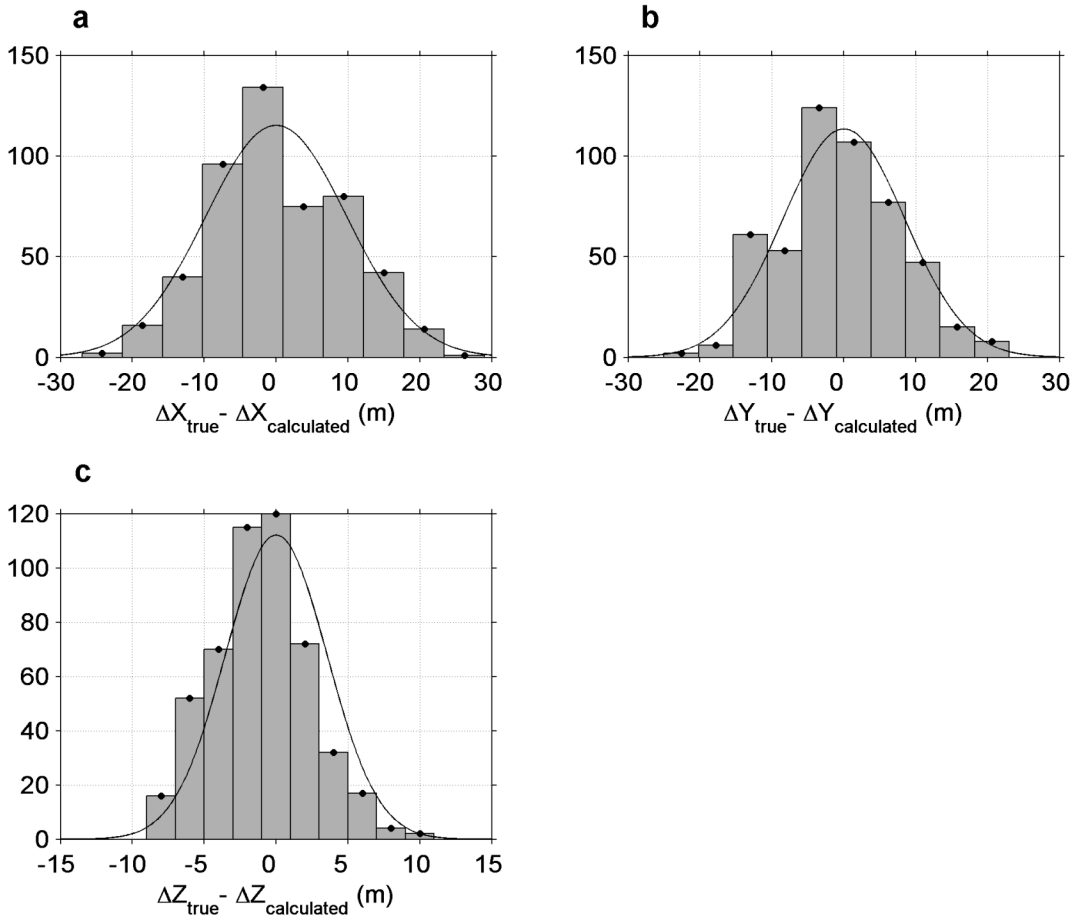

Figure 13. The three histograms represent the distribution of the relative errors in (a) x, (b) y, (c) z. A Gaussian distribution is fitted to each distribution. The standard deviation is found to be 10 meters in x, 8.5 meters in y and 4 meters in z.

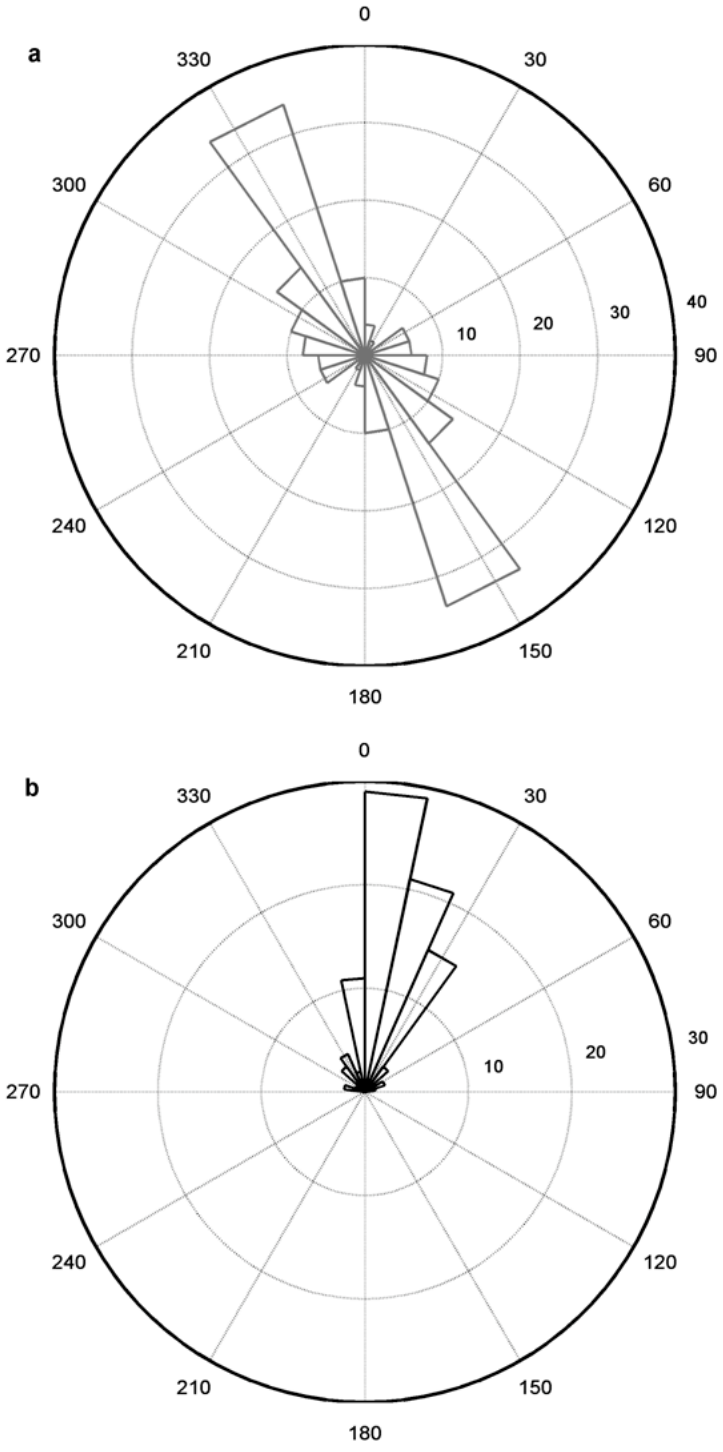

Figure 14. (a) Azimuth and (b) plunge in degrees of the planes deduced by planarity analysis. All the clusters have a planarity higher than 0.9. The majority of the planes have an azimuth of N155^{o}E and are horizontal or sub-horizontal with a plunge less than 30^{o}.

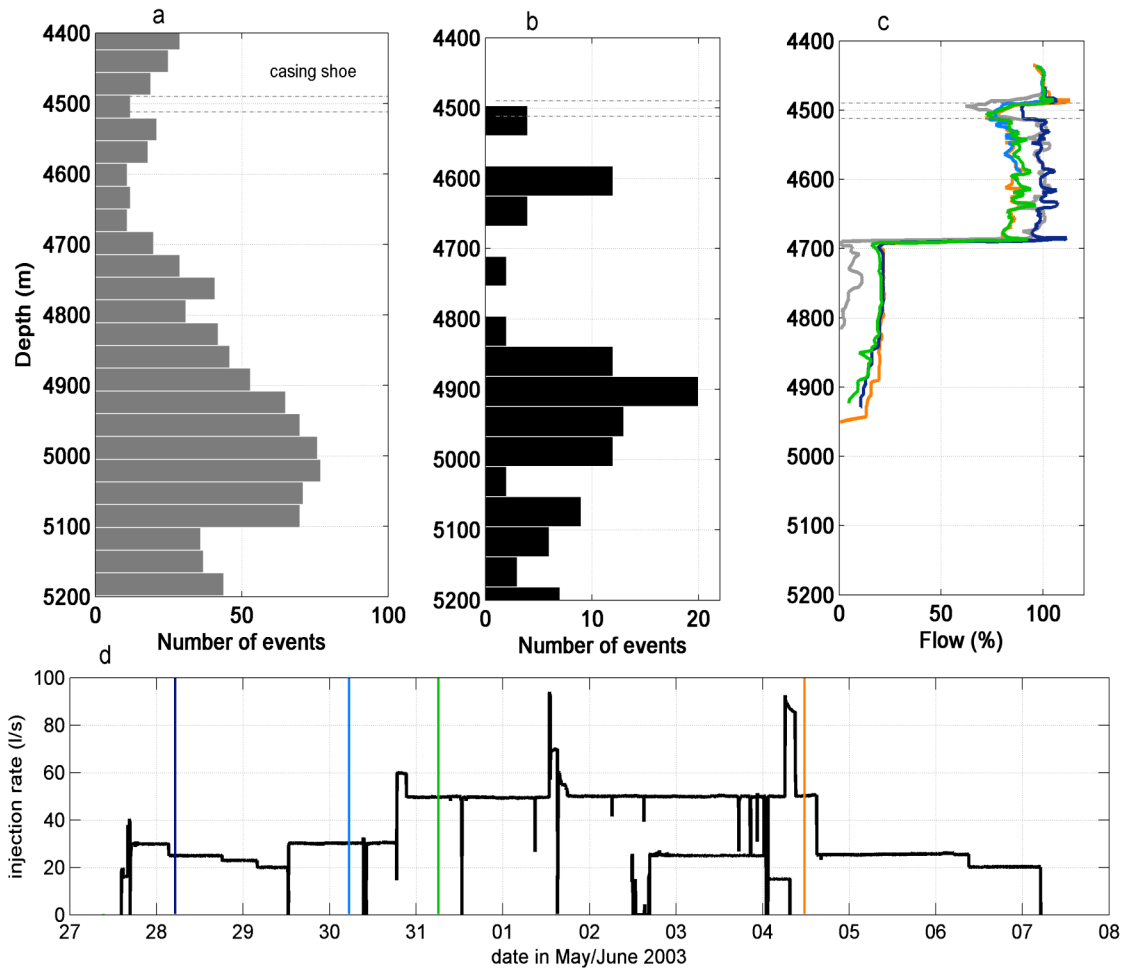

Figure 15. Depth distribution of **(a)** all events (collapsed) and **(b)** clustered events around the GPK3 well (300m around the well in average) respectively. The depth interval corresponds to the one of the flow log. **(c)** Flow log in the GPK3 well performed in 2003 at different times of the operations (Courtesy of D. Teza (BESTEC) and J. Nicholls). The flow as a percentage flowing to the well (i.e. 100% means no flow into the formation) is plotted versus depth. Different colors in 15c show flow rates at different stages of the stimulation. Gray is before stimulation. Other colors correspond to times indicated in 15d.